



Hot Dust-obscured Galaxies with Excess Blue Light

R. J. Assef¹ , M. Brightman² , D. J. Walton³ , D. Stern⁴ , F. E. Bauer^{5,6,7} , A. W. Blain⁸ , T. Díaz-Santos^{1,13,14},

P. R. M. Eisenhardt⁴, R. C. Hickox⁹ , H. D. Jun¹⁰, A. Psychogios^{11,14}, C.-W. Tsai¹², and J. W. Wu¹²

¹ Núcleo de Astronomía de la Facultad de Ingeniería y Ciencias, Universidad Diego Portales, Av. Ejército Libertador 441, Santiago, Chile

² Cahill Center for Astrophysics, California Institute of Technology, 1216 East California Boulevard, Pasadena, CA 91125, USA

³ Institute of Astronomy, University of Cambridge, Madingley Road, Cambridge CB3 0HA, UK

⁴ Jet Propulsion Laboratory, California Institute of Technology, 4800 Oak Grove Drive, Pasadena, CA 91109, USA

⁵ Instituto de Astrofísica, Facultad de Física, Pontificia Universidad Católica de Chile, 306, Santiago 22, Chile

⁶ Millennium Institute of Astrophysics (MAS), Nuncio Monseñor Sótero Sanz 100, Providencia, Santiago, Chile

⁷ Space Science Institute, 4750 Walnut Street, Suite 205, Boulder, CO 80301, USA

⁸ Physics & Astronomy, University of Leicester, 1 University Road, Leicester LE1 7RH, UK

⁹ Department of Physics and Astronomy, Dartmouth College, 6127 Wilder Laboratory, Hanover, NH 03755, USA

¹⁰ School of Physics, Korea Institute for Advanced Study, 85 Hoegiro, Dongdaemun-gu, Seoul 02455, Republic of Korea

¹¹ Department of Physics, University of Crete, 71003, Heraklion, Greece

¹² National Astronomical Observatories, Chinese Academy of Sciences, 20A Datun Road, Chaoyang District, Beijing, 100012, People's Republic of China

¹³ Chinese Academy of Sciences South America Center for Astronomy (CASSACA), National Astronomical Observatories, Chinese Academy of Sciences, Beijing, 100101, People's Republic of China

¹⁴ Institute of Astrophysics, Foundation for Research and Technology—Hellas (FORTH), Heraklion, GR-70013, Greece

Received 2019 April 25; revised 2020 May 26; accepted 2020 May 28; published 2020 July 8

Abstract

Hot dust-obscured galaxies (Hot DOGs) are among the most luminous galaxies in the universe. Powered by highly obscured, possibly Compton-thick, active galactic nuclei (AGNs), Hot DOGs are characterized by spectral energy distributions that are very red in the mid-infrared yet dominated by the host galaxy stellar emission in the UV and optical. An earlier study identified a subsample of Hot DOGs with significantly enhanced UV emission. One target, W0204–0506, was studied in detail and, based on Chandra observations, it was concluded that the enhanced emission was most likely due to either extreme unobscured star formation (star formation rate $> 1000 M_{\odot} \text{ yr}^{-1}$) or to light from the highly obscured AGN scattered by gas or dust into our line of sight. Here, we present a follow-up study of W0204–0506 as well as two more Hot DOGs with excess UV emission. For the two new objects we obtained Chandra/ACIS-S observations, and for all three targets we obtained Hubble Space Telescope/WFC3 F555W and F160W imaging. The analysis of these observations, combined with multiwavelength photometry and UV/optical spectroscopy suggests that UV emission is most likely dominated by light from the central highly obscured, hyperluminous AGN that has been scattered into our line of sight, by either gas or dust. We cannot decisively rule out, however, that star formation or a second AGN in the system may significantly contribute to the UV excess of these targets.

Unified Astronomy Thesaurus concepts: Active galaxies (17); Galaxy evolution (594); High-redshift galaxies (734); Quasars (1319); Infrared galaxies (790)

1. Introduction

Hot dust-obscured galaxies (Hot DOGs; Eisenhardt et al. 2012; Wu et al. 2012) are some of the most luminous galaxies in the universe, with bolometric luminosities $L_{\text{bol}} > 10^{13} L_{\odot}$ and a significant fraction with $L_{\text{bol}} > 10^{14} L_{\odot}$ (Wu et al. 2012; Tsai et al. 2015). Discovered by the Wide-field Infrared Survey Explorer (WISE; Wright et al. 2010), Hot DOGs are characterized by very red mid-IR colors and spectral energy distributions (SEDs) that peak at rest frame $\sim 20 \mu\text{m}$. This implies that Hot DOGs are powered by highly obscured, hyperluminous AGN that dominate the SED from the mid- to the far-IR (Eisenhardt et al. 2012; Wu et al. 2012, 2014; Díaz-Santos et al. 2016; Fan et al. 2016b; Tsai et al. 2018). As expected from their luminosities, Hot DOGs are rare, with one object every $31 \pm 4 \text{ deg}^2$. Yet their number density is comparable to that of similarly luminous unobscured quasars (Assef et al. 2015) and of heavily reddened type 1 quasars (Banerji et al. 2015).

X-ray studies have shown that the obscuration of the central engine in Hot DOGs is very high, with column densities ranging from somewhat below to above the Compton-thick limit (i.e., $N_{\text{H}} > 1.5 \times 10^{24} \text{ cm}^{-2}$; Stern et al. 2014;

Piconcelli et al. 2015; Assef et al. 2016; Ricci et al. 2017; Vito et al. 2018). As the AGN emission is highly obscured, the host galaxy is observable at rest-frame UV, optical, and near-IR wavelengths. A study of their SEDs by Assef et al. (2015) showed that their stellar masses, as derived from their rest-frame near-IR luminosities, imply that either the supermassive black holes (SMBHs) are accreting well above the Eddington limit, or that their SMBH masses (M_{BH}) are well above the local relations between M_{BH} and the mass of the spheroidal component of the host galaxy (see, e.g., Magorrian et al. 1998; Bennert et al. 2011). Indeed, recent results by Wu et al. (2018) and Tsai et al. (2018) suggest that Hot DOGs are radiating at or above the Eddington limit, which in turn suggests that Hot DOGs are likely experiencing strong AGN feedback that could easily affect the whole host galaxy and its immediate environment. Indeed, Díaz-Santos et al. (2016) presented a study of the [C II] $157.7 \mu\text{m}$ emission line in the highest luminosity Hot DOG, and possibly the most luminous galaxy known, WISEA J224607.56–052634.9 (W2246–0526; Tsai et al. 2015), and determined based on the emission-line kinematics that the central gas of the host galaxy is likely undergoing an isotropic outflow event. Additional ionized gas

outflow signatures have been observed in the optical narrow emission lines of some other Hot DOGs (Wu et al. 2018; Jun et al. 2020), supporting the presence of strong AGN feedback in the interstellar medium (ISM) of these targets.

Assef et al. (2015, also see Eisenhardt et al. 2012; Tsai et al. 2015, 2018) showed that the UV through mid-IR SED of the majority of Hot DOGs (specifically “W12–drops” with $z > 1$) can be well modeled as a combination of a star-forming galaxy that dominates the optical/UV emission, and a luminous, obscured AGN that dominates the mid-IR SED and the bolometric luminosity of the system. However, this is not the case for all Hot DOGs. In a later work, Assef et al. (2016, A16 hereafter) presented a small sample of eight Hot DOGs whose optical/UV emission is not well modeled by a star-forming galaxy, but instead needs a second, unobscured AGN component that is only $\sim 1\%$ as luminous as the obscured component. A16 posited that the SED could be explained by three different scenarios: (i) that the UV/optical emission is dominated by leaked or scattered light from the hyperluminous, highly obscured AGN; (ii) that the system is a dual quasar, with a more luminous, highly obscured quasar and a less luminous, unobscured one; and (iii) that the system is undergoing an extreme star formation event with little dust obscuration such that the broadband UV/optical SED is similar to that of an AGN.

One of these objects, WISEA J020446.13–050640.8 (W0204–0506 hereafter), was serendipitously observed by the Chandra X-ray Observatory as part of the Large-Area Lyman Alpha survey (Rhodes et al. 2000). A16 studied this object in detail using these observations along with broadband SED and optical spectroscopic observations. A16 determined that the X-ray spectrum of W0204–0506 is consistent with a single, hyperluminous, highly absorbed AGN ($\log L_{2-10 \text{ keV}}/\text{erg s}^{-1} = 44.9^{+0.86}_{-0.14}$, $N_{\text{H}} = 6.3^{+8.1}_{-2.1} \times 10^{23} \text{ cm}^{-2}$), and highly inconsistent with a secondary, unobscured AGN with the luminosity necessary to explain the optical/UV emission. Instead, A16 found that the UV/optical continuum was better explained by a starburst with a star formation rate $\gtrsim 1000 M_{\odot} \text{ yr}^{-1}$, or by scattered light from the hyperluminous, highly obscured central engine. While star formation rates (SFRs) $\gtrsim 1000 M_{\odot} \text{ yr}^{-1}$ are routinely found through far-IR/submillimeter observations of highly obscured systems such as SMGs and ULIRGs, rates above $\sim 300 M_{\odot} \text{ yr}^{-1}$ have never been observed through UV/optical wavelengths in Lyman break galaxies, which have the strongest UV/optical star formation rates measured (Barger et al. 2014). Due to the large SFR needed to explain the optical/UV SED of this object as a starburst, A16 favored the scattered AGN light scenario.

In this paper we present Hubble Space Telescope (HST) observations of W0204–0506 to further explore its nature, and we explore in detail two more blue excess Hot DOGs (BHDs), WISE J022052.12+013711.6 (W0220+0137 hereafter) and WISE J011601.41–050504.0 (W0116–0505 hereafter), using HST and Chandra observations as well as optical spectroscopy and broadband UV through mid-IR SEDs. In Section 2 we present the sample studied here as well as the different observations available for each target, and describe the SED modeling done by A16 to identify these unusual objects. In Section 3 we discuss the modeling of the Chandra X-ray observations. In Section 4 we present a detailed discussion of the source of the excess blue emission, analyzing each possible scenario in light of the available observations. Our conclusions are summarized in Section 5. Throughout the article all

magnitudes are presented in their natural system unless otherwise stated, namely AB for $ugriz$ and Vega for all the rest. We assume a concordance flat Λ CDM cosmology with $H_0 = 70 \text{ km s}^{-1} \text{ Mpc}^{-1}$, $\Omega_{\Lambda} = 0.7$, and $\Omega_M = 0.3$. For all quantities derived from X-ray spectra, we quote 90% confidence intervals, while for all other quantities we quote 68.3% confidence intervals instead.

2. Sample and Observations

2.1. BHDs

A16 identified 8 BHDs from a sample of 36 Hot DOGs with WISE W4 < 7.2 mag, spectroscopic redshifts $z > 1$, and $ugriz$ modelMag¹⁵ photometry in the Sloan Digital Sky Survey (SDSS) DR12 database with signal-to-noise ratio (S/N) > 3 in at least one of the SDSS bands. This spectroscopic sample is biased toward optical emission, and after considering the selection effects, A16 estimated BHDs could comprise as much as 8% of the Hot DOG population with W4 < 7.2 mag, although most likely a smaller fraction when considering fainter W4 fluxes.

To select this sample, A16 started by modeling the SEDs of the aforementioned 36 Hot DOGs using the galaxy and AGN SED templates and modeling algorithm of Assef et al. (2010), following the prescription presented by Assef et al. (2015). In short, the broadband SED of any given object was modeled as a linear, nonnegative combination of four empirically derived SED templates: an “E” template, which resembles the SED of an old stellar population, an “Sbc” template, which resembles the SED of an intermediately star-forming galaxy, an “Im” template, which resembles a local starburst galaxy, and a type 1 AGN template. The reddening of the AGN template, parameterized by $E(B - V)$, was also fit for, assuming $R_V = 3.1$ and a reddening law that follows that of the SMC at short wavelengths but that of the Milky Way at longer wavelengths. A single intergalactic medium absorption strength was also fit for all templates when needed (see Assef et al. 2010, 2015, A16 for details). Using this approach A16 modeled the SED of each object in the following broad bands: the $ugriz$ SDSS DR12 modelMag photometry, Spitzer/IRAC [3.6] and [4.5] photometry from Griffith et al. (2012), and the WISE W3 and W4 photometry from the WISE All-Sky Data Release (Cutri et al. 2012). Additionally, whenever possible, A16 used the J , K_s , and deeper r -band imaging presented by Assef et al. (2015). For the three sources considered in this article, the deeper r -band imaging was obtained using the 4.1 m Southern Astrophysical Research Telescope (SOAR) with the SOAR Optical Imager (SOI). For W0116–0505, images were obtained with an exposure time of 3×600 s on the night of UT 2013 August 28. For the other two sources, the images were obtained on UT 2011 November 20, with exposure times of 3×500 s for W0204–0506 and of 2×500 s for W0220+0137. In all cases the images were reduced following standard procedures, and the photometric calibration was performed by comparing bright stars in each field with their respective SDSS magnitudes. The details of the near-IR imaging can be found in Assef et al. (2015). All magnitudes are shown in Table 1.

A16 found that the approach described above was not able to accurately model the UV/optical emission for a fraction of their sample, which were significantly bluer than allowed by

¹⁵ http://www.sdss.org/dr12/algorithms/magnitudes/#mag_model

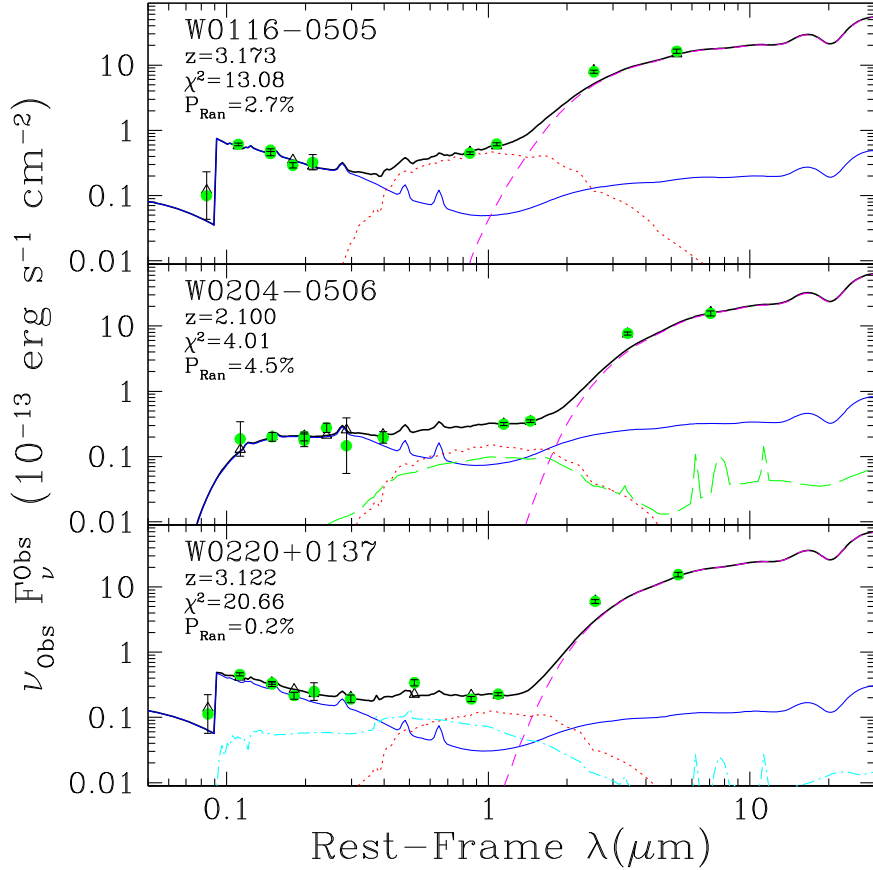


Figure 1. UV through mid-IR SEDs of the three BHs discussed in this study, identified by their SEDs as discussed in the text. We only show the photometric data used to identify these targets as BHs by A16. The green solid points show the observed flux densities in the photometric bands discussed in Section 2.1. The solid black line shows the best-fit SED model to the photometric data points, which consists of a nonnegative linear combination of a primary luminous, obscured AGN (dashed magenta line), a secondary less luminous, unobscured or mildly obscured AGN (solid blue line), an old stellar population (dotted red line), an intermediate stellar population (dashed green line), and a young stellar population (cyan dotted-dashed line). The open triangles show the predicted flux density for each photometric band based on the best-fit SED model. For each object we indicate also the redshift and the probability P_{Ran} that the improvement in χ^2 gained from adding the secondary AGN component is spurious.

Table 1
Photometric Data

WISE ID	J011601.41-050504.0	J020446.13-050640.8	J022052.12+013711.6
SDSS <i>u</i>	23.571 ± 0.685	23.004 ± 0.600	23.470 ± 0.587
SDSS <i>g</i>	21.464 ± 0.054	22.660 ± 0.166	21.779 ± 0.059
F555W	21.679 ± 0.019	22.441 ± 0.047	21.772 ± 0.018
SDSS <i>r</i>	21.383 ± 0.054	22.488 ± 0.234	21.841 ± 0.086
SOI <i>r</i>	21.515 ± 0.078	22.357 ± 0.166	21.803 ± 0.047
SDSS <i>i</i>	21.740 ± 0.094	21.797 ± 0.175	22.060 ± 0.132
SDSS <i>z</i>	21.368 ± 0.257	22.026 ± 0.667	21.607 ± 0.273
<i>J</i>	...	20.768 ± 0.216	20.790 ± 0.149
F160W	20.648 ± 0.007	20.390 ± 0.007	21.077 ± 0.010
<i>Ks</i>	18.604 ± 0.117
W1	17.130 ± 0.184	17.343 ± 0.115	17.875 ± 0.225
[3.6]	16.800 ± 0.040	17.182 ± 0.056	17.722 ± 0.091
[4.5]	15.725 ± 0.021	16.340 ± 0.033	16.806 ± 0.051
W2	15.564 ± 0.156	16.103 ± 0.158	16.575 ± 0.253
W3	10.213 ± 0.059	10.245 ± 0.056	10.512 ± 0.075
W4	7.014 ± 0.084	7.062 ± 0.090	7.076 ± 0.092

the SED templates. They identified eight objects for which an additional, secondary AGN component with independent normalization and reddening provided a significant improvement in χ^2 to the best-fit SED model. A16 presented a detailed

study of the properties of one of these targets: W0204-0506. Here we study an additional one of these eight targets, W0220+0137, as well as another very similar target, W0116-0505. The $W1 = 17.13 \pm 0.18$ mag of W0116-0505 is slightly

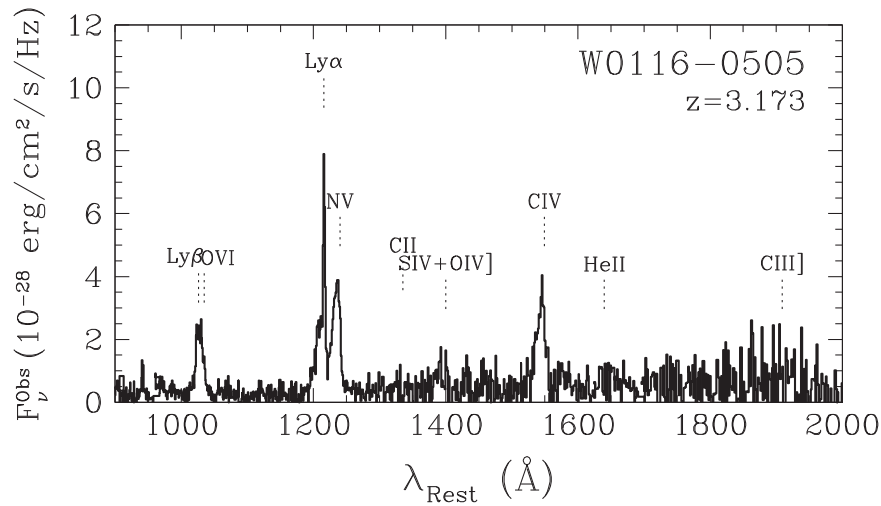


Figure 2. Optical spectrum of W0116–0505 from SDSS.

Table 2
Best-fit SED Parameters

Object	Redshift	Primary AGN		Secondary AGN		
		$\log L_{6\mu\text{m}}$ (erg s $^{-1}$)	$E(B - V)$ (mag)	$\log L_{6\mu\text{m}}$ (erg s $^{-1}$)	$E(B - V)$ (mag)	P_{ran} (10 $^{-2}$)
W0116–0505	3.173	$47.24^{+0.17}_{-0.11}$	$4.24^{+2.71}_{-1.23}$	$45.18^{+0.04}_{-0.03}$	$0.00^{+0.02}_{-0.00}$	2.7
W0204–0506	2.100	$46.87^{+0.03}_{-0.08}$	$10.00^{+1.74}_{-2.06}$	$44.98^{+0.04}_{-0.22}$	$0.10^{+0.00}_{-0.05}$	4.5
W0220+0137	3.122	$47.33^{+0.16}_{-0.16}$	$7.33^{+2.67}_{-2.32}$	$44.96^{+0.08}_{-0.11}$	$0.00^{+0.02}_{-0.00}$	0.2

Note. The uncertainties have been derived through a Monte-Carlo process, as described in the text, and hence do not capture the possible systematic uncertainties described at the end of Section 2.1.

brighter than the formal Hot DOG selection limit ($W1 > 17.4$; Eisenhardt et al. 2012), and hence it was excluded from the final list presented by A16 despite meeting all other selection criteria. We find there is only a 2.7% probability that the improvement in χ^2 by the secondary AGN component is spurious for this source. A16 argued that these probabilities are likely overestimated and hence conservative, as the F-test used to estimate them does not take into account the constraints provided by the nonnegative requirement of the linear combination of templates for the best-fit model.

The broadband SEDs as well as the best-fit SED models of the three targets are shown in Figure 1. We note that the SED of W0204–0506 differs slightly from that presented by A16 as, for consistency with the other two sources, the SED presented here only uses the SDSS DR12 bands in the UV/optical instead of the deeper imaging of Finkelstein et al. (2007). Table 2 shows, for each target, the best-fit $E(B - V)$ to both the primary and secondary AGN components, and Figure 1 shows the best-fit SED models. The table also shows the reddening-corrected monochromatic luminosities at $6\mu\text{m}$, $L_{6\mu\text{m}}$, calculated from the template fit to each AGN component. The uncertainties for the parameters shown in Table 2 have been estimated using a Monte-Carlo method following a similar prescription to that used by A16. For each object we first apply a scaling factor to the photometric uncertainties such that the best-fit SED model has a reduced χ^2 (χ^2_ν) of 1. We then create 1000 realizations of the observed SED of each object by re-sampling its photometry according to

these scaled uncertainties and assuming a Gaussian distribution. We fit each of the 1000 simulated SEDs and compile the distribution of each parameter. We assign the uncertainties to the 68.3% intervals of these distributions around the values of the best-fit model.

As the set of templates used is limited, we warn the reader that we may have neglected significant systematic uncertainties. For example, Figure 1 shows that the best-fit SED models have a significant contribution from the old stellar population template, which could be at odds with the young age of the universe at the redshift of these objects. However, it should be noted that because in the Assef et al. (2010) algorithm SEDs are modeled by linear combinations of three empirical templates, stellar population ages should not be associated to any specific template, but rather to the combination of them. Furthermore, the host emission is only constrained by the rest-frame near-IR and hence is insensitive to the star formation history of the underlying stellar population. This will naturally lead to a significant degeneracy in the host galaxy SED modeling. As a test, we re-fit the SEDs excluding old stellar populations. The best-fit parameters listed in Table 2 are all within the estimated uncertainties, and the P_{Ran} values all become somewhat smaller (by factors of ~ 3), indicating that our results are qualitatively unaffected. Similarly, systematics in determining the AGN luminosities may also have been neglected. A detailed analysis of the dust emission SED of Hot DOGs, including data from Herschel, will be presented

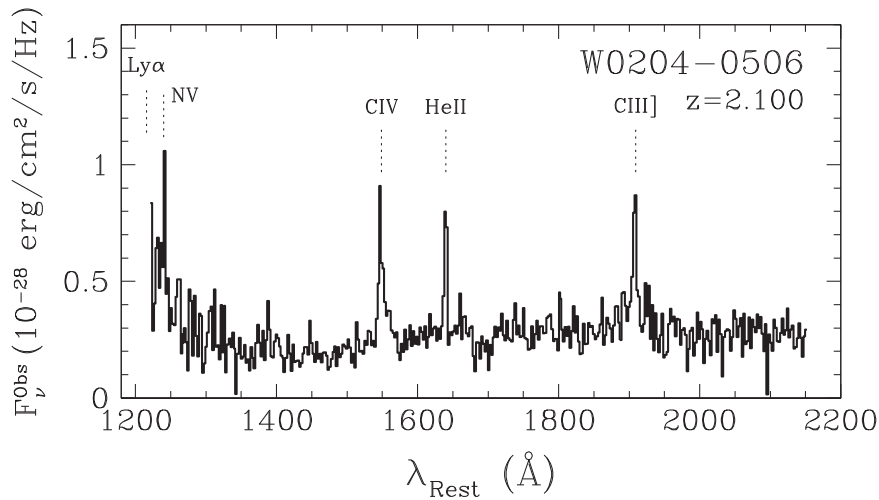


Figure 3. Optical spectrum of W0204–0506, obtained with the GMOS-S instrument at the Gemini South Observatory.

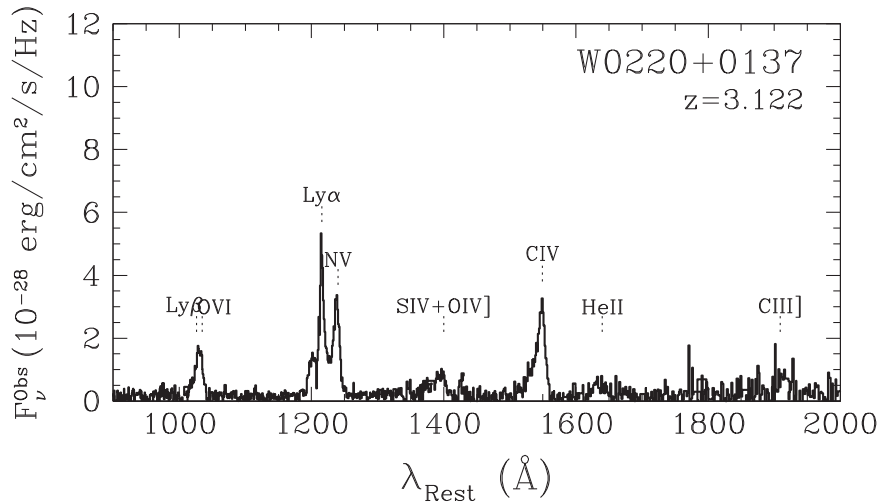


Figure 4. Optical spectrum of W0220+0137 from SDSS.

elsewhere and will elucidate this issue further (C.-W. Tsai et al. 2020, in preparation).

2.2. Optical Spectra

The optical spectra of W0116–0505, W0204–0506, and W0220+0137 are presented in Figures 2–4, respectively. For W0116–0505 and W0220+0137, the spectra were obtained from SDSS. The optical spectrum of W0204–0506 was obtained using the GMOS-S spectrograph on the Gemini South telescope on UT 2011 November 27 using a longslit with a width of $1''.5$ as well. These observations have been previously presented by A16, and we refer the reader to that study for further details on these observations. The spectra of W0116–0505 and W0220+0137 show broad high-ionization emission lines typically observed in luminous quasars. W0204–0506, on the other hand, has a spectrum more similar to obscured, or type 2, quasars such as high-redshift radio galaxies (e.g., Stern et al. 1999; de Breuck et al. 2001) and other radio-quiet (or non-radio-selected) quasars at high redshift (e.g., Stern et al. 2002; Hainline et al. 2012; Alexandroff et al. 2013). Single Gaussian fits to the CIV emission line, following the prescription of Assef et al. (2011, and references therein) to fit the continuum and define the

spectral region on which to fit the emission line, have FWHM of approximately 2800 km s^{-1} and 3500 km s^{-1} , respectively for W0116–0505 and W0220+0137. Based on these emission lines, we measure a redshift of $z = 3.173 \pm 0.002$ for W0116–0505, and $z = 3.122 \pm 0.002$ for W0220+0137. In particular both spectra show blended Ly β and O VI emission features. W0204–0506 is at a significantly lower redshift of $z = 2.100 \pm 0.002$, and hence we cannot determine if these emission lines are present in the spectrum, as they fall shortward of the atmospheric UV cut-off.

2.3. HST Observations

A joint program between Chandra and HST was approved during Chandra Cycle 17 (PID 17700696) to obtain HST imaging in two bands of all three targets and to obtain Chandra/ACIS-S observations of W0116–0505 and W0220+0137. These targets were selected for having some of the clearest blue excess emission in terms of the χ^2 improvement, and for having some of the highest expected count rates in ACIS-S. The archival Chandra/ACIS-I observations for W0204–0506 presented by A16 are sufficient to accomplish our science goals, so no further observations were requested. In

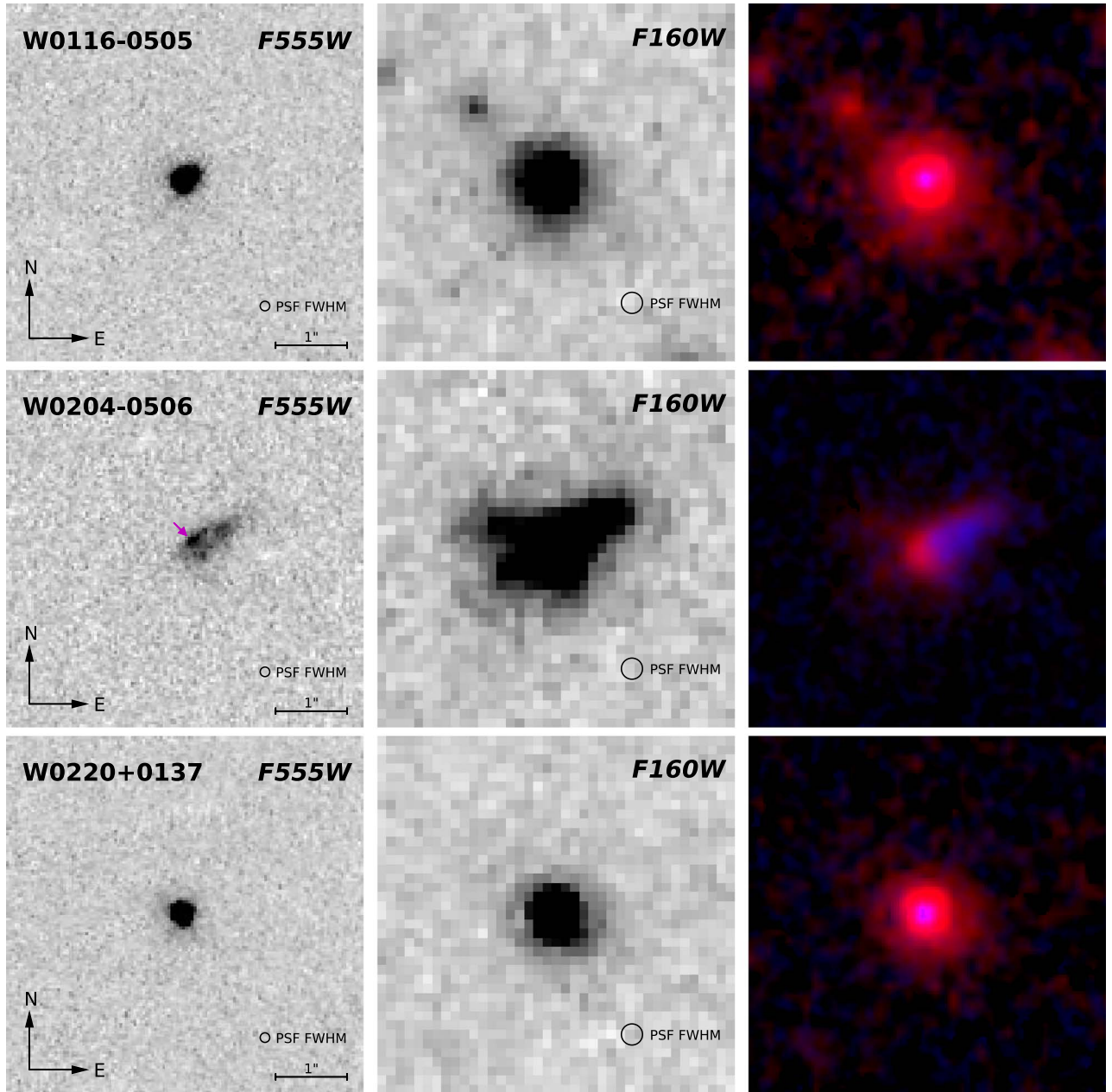


Figure 5. HST/WFC3 images of W0116–0505 (top row), W0204–0506 (middle row), and W0220+0137 (bottom row) in the F555W (left panels) and F160W (middle panels) bands. The right panels show a color composite where the F160W band has been mapped to red and the F555W band has been mapped to blue, and we have matched the point-spread function of the F555W band to that of F160W. Each panel shows a $5'' \times 5''$ region centered on the F160W centroid of each target.

this section we focus on the HST observations, while the Chandra observations are described in the next section.

Imaging observations of all three BHD targets were obtained using the WFC3 camera on board HST in both the F555W and the F160W bands. Each target was observed during one orbit, with two exposures in the F555W band followed by three exposures in the F160W band. The exposure times in the F555W band were 738 s and 626 s for each image for W0116–0505 and W0204–0506, and 735 s and 625 s each for W0220+0137. All exposure times in the F160W band were 353 s. For the F160W band we use the reduced images provided by the HST archive. Cutouts of $5'' \times 5''$ centered on the F160W coordinates of the target are shown in the middle panels of Figure 5.

For the F555W band we do not use the archive-provided reductions, as the pipeline cosmic-ray rejection is significantly compromised by the acquisition of only two images. Instead, we take the fully reduced single frames provided by the archive, including the charge transfer efficiency correction, and use the LACOSMIC algorithm (van Dokkum 2001) to remove cosmic rays. We then use those cosmic-ray corrected images to continue with the pipeline processing and combine the frames. We align the F555W image to the F160W image using stars detected in both bands. The final images are shown in the left panels of Figure 5. Table 1 presents the $4''$ diameter aperture magnitudes measured in each band for each object.

The right panels of Figure 5 show a color composite of the images created using the Lupton et al. (2004) algorithm as

Table 3
Morphology of Blue Excess Hot DOGs

Source	Band	Gini	M_{20}	A
W0116–0505	F555W	0.499 ± 0.003	-2.00 ± 0.16	0.133 ± 0.010
	F160W	0.527 ± 0.008	-2.08 ± 0.02	0.116 ± 0.049
W0204–0506	F555W	0.529 ± 0.016	-1.19 ± 0.14	0.599 ± 0.027
	F160W	0.633 ± 0.011	-0.81 ± 0.02	0.278 ± 0.010
W0220+0137	F555W	0.491 ± 0.004	-1.77 ± 0.09	0.112 ± 0.009
	F160W	0.559 ± 0.016	-2.16 ± 0.04	0.172 ± 0.016

implemented through the `astropy v2.0.1`¹⁶ function `make_lupton_rgb`. We assign the F555W image to the blue channel and the F160W image to the red channel, while leaving the green channel empty. Before producing the composite image, we convolve the F555W image with a Gaussian kernel to match its point-spread function (PSF) to that of the F160W image. We assume that the PSFs of both images are well modeled by Gaussian PSFs with the respective FWHMs as provided by the WFC3 documentation,¹⁷ namely $0.^{\circ}067$ for the F555W channel, and $0.^{\circ}148$ for the F160W channel. Hence, the Gaussian kernel used on the F555W image corresponds to a Gaussian function with $\text{FWHM}_{\text{kernel}}^2 = \text{FWHM}_{\text{F160W}}^2 - \text{FWHM}_{\text{F555W}}^2$.

The emission of the three objects is clearly resolved in both bands. For W0116–0505 and W0220+0137 the morphologies seem to be broadly undisturbed in both bands, with the F160W emission having a larger extent and a higher luminosity. The emission peaks in both bands are spatially colocated. W0204–0506 is, on the other hand, quite clearly disturbed, with the F160W morphology (rest frame 5200 \AA) suggestive of a recent interaction. The F555W emission (rest frame 1800 \AA) is patchy, reminiscent of a starburst. We discuss the implications of this UV morphology further in Section 4.

To more quantitatively assess the morphology of these sources, we have measured different coefficients commonly used in the literature. Specifically, we follow Lotz et al. (2004) to measure the Gini, M_{20} , and A coefficients (Lotz et al. 2004, and references therein). The Gini coefficient (Abraham et al. 2003) measures how uniformly distributed is the light among the pixels of a galaxy in an image, such that Gini is 0 if all pixels have a uniform brightness and 1 if all the brightness is concentrated in a single pixel. The M_{20} coefficient measures the second order moment of the brightest 20% of the flux of the galaxy as compared to the total second order moment, M_{tot} . The moments are computed around a center chosen to minimize M_{tot} . The A coefficient measures the rotational asymmetry of a galaxy by subtracting an image of the galaxy rotated by 180° . The rotational center is chosen to minimize A. For further details on these coefficients, we refer the reader to Lotz et al. (2004) and Conselice (2014).

We start by subtracting the background using `SExtractor` (v2.19.5, Bertin & Arnouts 1996) as well as obtaining the centroid of each object in each band. We then compute the Petrosian radius (Petrosian 1976) and generate the segmentation map following Lotz et al. (2004), and finally proceed to measure the coefficients discussed above. The values and uncertainties of the Gini, M_{20} , and A coefficients for each

object in each band are shown in Table 3. We estimate the uncertainties in each parameter through a Monte-Carlo approach. For a given object in a given band, we use the uncertainty in each pixel to generate 1000 resampled images assuming Gaussian statistics. We then repeat the measurement in each resampled image following the procedure outlined above. We assign the measurement error to be the dispersion of the coefficient measurements in the 1000 resampled images.

Recently, Farrah et al. (2017) measured these coefficients for 12 Hot DOGs using HST/WFC3 images in F160W. Using the boundaries proposed by Lotz et al. (2004) in the Gini–A plane and by Lotz et al. (2008) in the Gini– M_{20} plane, Farrah et al. (2017) determined that while Hot DOGs have a high merger fraction ($\sim 80\%$), this fraction is consistent with that found for massive galaxies at $z \sim 2$, leading them to conclude that Hot DOGs are not preferentially associated with mergers. These results are generally consistent with those of Fan et al. (2016a), who also found a high merger fraction ($62 \pm 14\%$) among Hot DOGs, as well as with those recently presented by Díaz-Santos et al. (2018), who found evidence with Atacama Large Millimeter/submillimeter Array $\sim 200 \mu\text{m}$ imaging of a triple major merger in the the most luminous Hot DOG, W2246–0526. If we adopt the same boundaries used by Farrah et al. (2017) to classify our sources according to their F160W morphologies, and note that all caveats identified by Farrah et al. (2017) also apply here, we find that the host galaxies of W0116–0505 and W0220+0137 are not consistent with mergers but instead are classified as undisturbed early-type galaxies. For W0204–0506, on the other hand, we find that its host galaxy morphology is best classified as an ongoing merger. These results are consistent with our visual characterization of the host galaxies.

2.4. Chandra Observations

We have obtained Chandra/ACIS-S observations of two of our targets: W0116–0505 and W0220+0137 (proposal ID 17700696). Each object was observed with a total exposure time of 70 ks. W0116–0505 was observed continuously, while the observations of W0220+0137 were split into one 30 ks and two 20 ks visits spread throughout seven days. It is worth noting that these observations have previously been presented by Vito et al. (2018) in the context of a larger sample of Hot DOGs observed in X-rays. They find both sources are heavily absorbed at those wavelengths. Goulding et al. (2018) analyzed the observations for W0220+0137 as well, but in the context of a large sample of Extremely Red Quasars (ERQs), and also found the source to be heavily absorbed at X-ray energies, which is qualitatively consistent with the rest of the ERQ population analyzed. Here we analyze the data following the approach of A16, who analyzed the archival Chandra/ACIS-I observations of W0204–0506.

¹⁶ <http://www.astropy.org/>

¹⁷ http://www.stsci.edu/hst/wfc3/documents/handbooks/currentHB/c06_uvis07.html#391868, http://www.stsci.edu/hst/wfc3/ins_performance/ground_components/filters

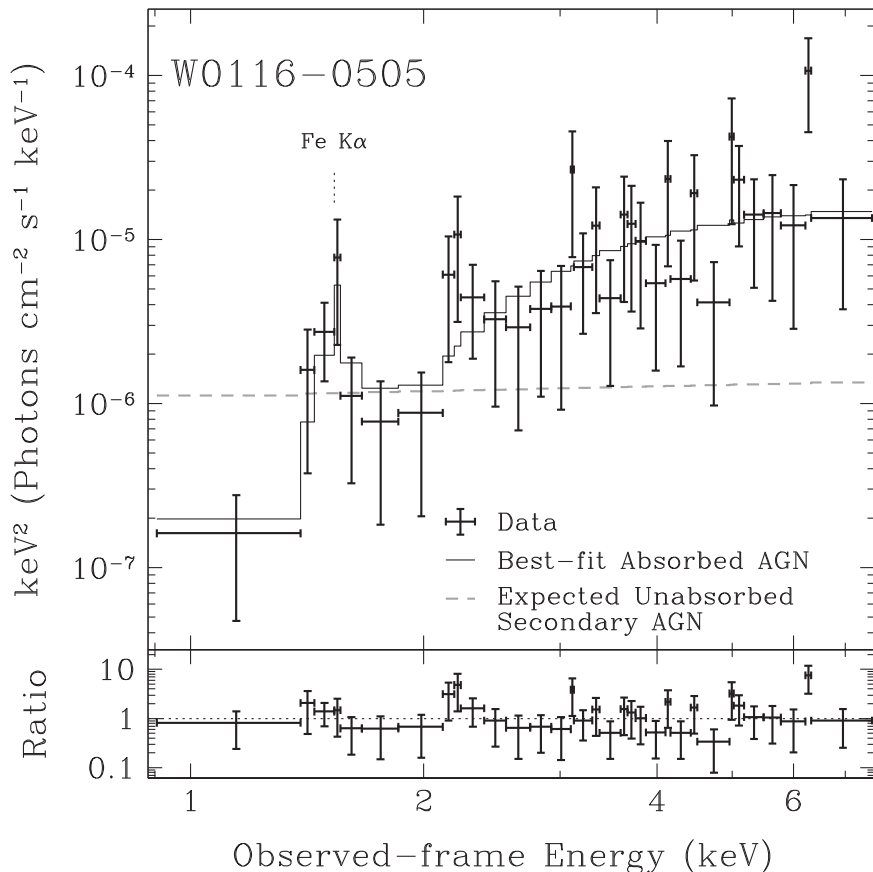


Figure 6. (Top panel) Unfolded X-ray spectrum of W0116–0505 obtained using Chandra/ACIS-S (see Section 2.4 for details). The solid black line shows the best-fit absorbed AGN model to the spectrum, as described in Section 3. The dashed-gray line shows the emission expected for a second, unobscured AGN in the system powering the observed UV/optical emission. (Bottom panel) The data points show the ratio between the observed spectrum and the best-fit model.

We use CIAO v4.7 to analyze these data. The spectral data products, including the source and background spectra, and the response files are created using the `specextract` tool. Source events are extracted from circular regions with 2'' radii centered on the source, while background events are extracted from annuli with inner and outer radii of 3 and 6'', respectively. For W0220+0137, the spectral products from the three observations are combined into one using the tool `combine_spectra`. We confirm that combining the spectral products in this way does not systematically affect our results by fitting the spectra of each individual obsID simultaneously, linking the fit parameters between them. We find consistent results compared to fitting the combined spectral products and proceed with the combined products. We use the HEASOFT tool `grppha` to group the spectra with a minimum of one count per bin.

After subtracting the background, 74 counts are detected for W0116–0505, and only 18 for W0220+0137. Figures 6 and 8 show their respective unfolded spectra. Note that the spectra have only been unfolded for the benefit of their presentation. For reference, we also show the ACIS-I spectrum of W0204–0506 in Figure 7, which had a significantly longer exposure time of 160 ks. The shape of all three spectra differ significantly from that of an unabsorbed power law, suggesting the emission is dominated by a highly obscured AGN, as expected from the SED modeling presented in Section 2.1. In the next section we model these spectra and discuss their implications for the nature of the BHs.

3. X-Ray Data Modeling

The X-ray spectra of W0116–0505 and W0220+0137 are clearly hard, implying the emission is most likely dominated by a highly obscured AGN. To better constrain the properties of the obscured AGN, we fit the emission of both objects using the models of Brightman & Nandra (2011), following the same approach as in A16. These models predict the X-ray spectrum as observed through an optically thick medium with a toroidal geometry, as posited by the AGN unified scheme. The models employ Monte-Carlo techniques to simulate the transfer of X-ray photons through the optically thick neutral medium, self-consistently including the effects of photoelectric absorption, Compton scattering, and fluorescence from Fe K, among other elements. Treating these effects self-consistently rather than separately has the advantage of reducing the number of free parameters and of gaining constraints on the spectral parameters. It is therefore particularly useful for low count spectra such as those we are fitting here. We therefore carry out the parameter estimation by minimizing the Cash statistic (Cash 1979), modified through the W-statistic provided by XSPEC¹⁸ to account for the subtracted background. Also following the approach of A16, we require the photon index Γ to be ≥ 1.6 , as it is poorly constrained by our data, and lower values are only appropriate for low Eddington ratios. In practice, the fitting procedure we use allows values of Γ in the range 1.6–3.0, and values of N_{H} in the range 10^{20} – 10^{26} cm⁻².

¹⁸ <https://heasarc.gsfc.nasa.gov/xanadu/xspec/manual/XSappendixStatistics.html>

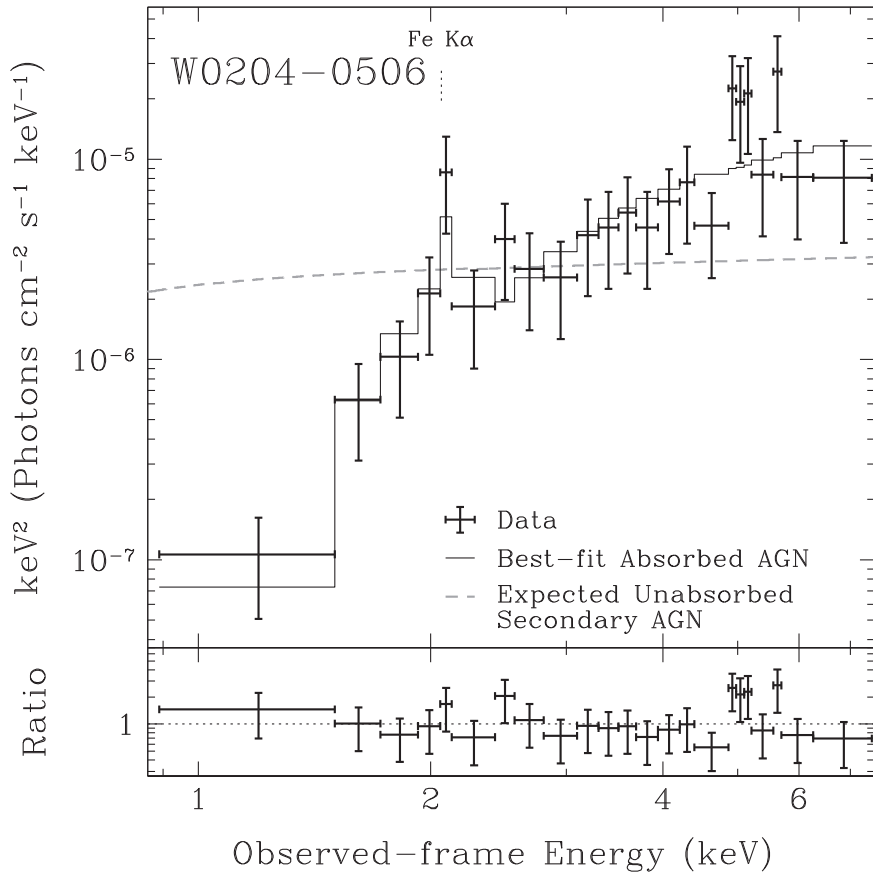


Figure 7. Same as Figure 6 but for the Chandra/ACIS-I spectrum of W0204–0506. Adapted from Figure 4 of A16.

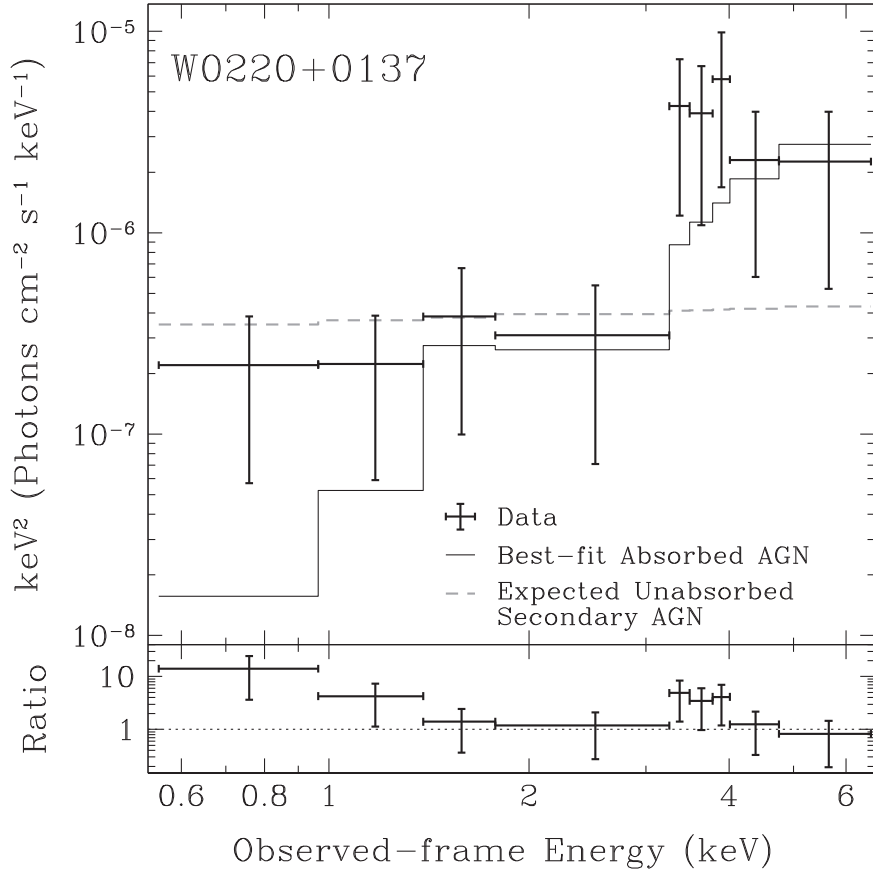


Figure 8. Same as Figure 6 but for the Chandra/ACIS-S spectrum of W0220+0137.

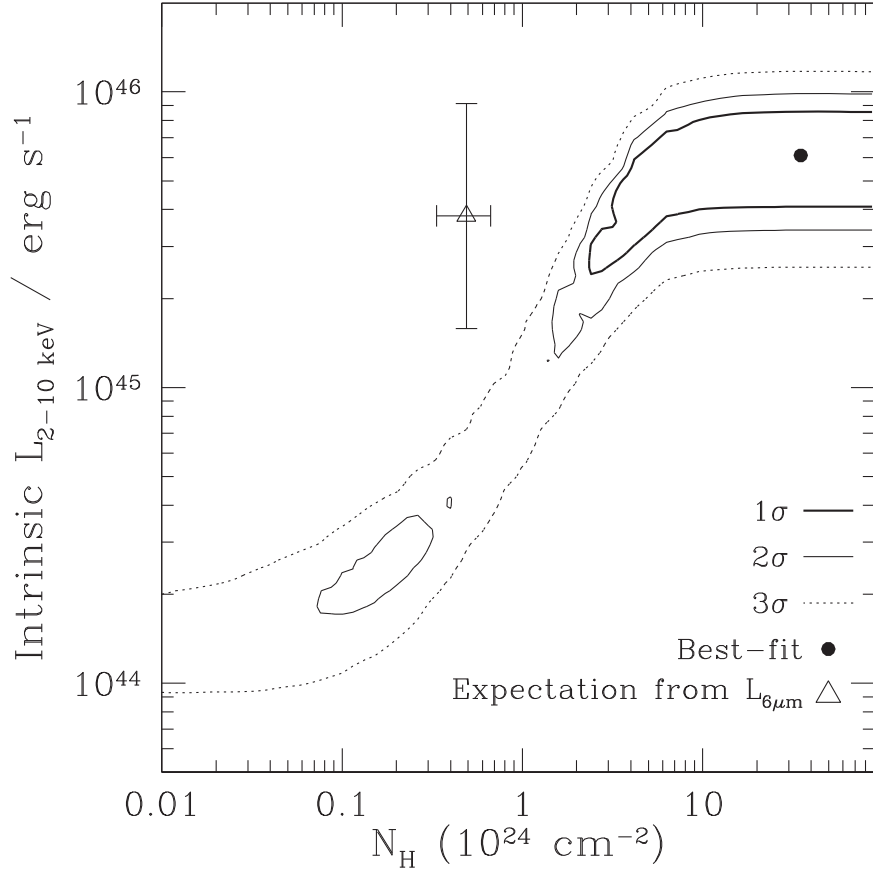


Figure 9. Confidence intervals of the fit to the Chandra/ACIS-S spectrum of W0220+0137 as described in the text.

However, for W0220+0137, there are too few counts to constrain all spectral parameters; therefore we fix Γ to the canonical value of 1.9, leaving only N_{H} and the normalization free.

Figures 6 and 8 show the best-fit models to the spectra of W0116–0505 and W0220+0137, respectively. The best-fit absorbed AGN model to W0116–0505 has an absorption column density of neutral hydrogen of $N_{\text{H}} = 1.2_{-0.7}^{+1.0} \times 10^{24} \text{ cm}^{-2}$, a photon index of $\Gamma = 1.9_{-0.7}^{+0.7}$ (where $-l$ signifies that the parameter is bound by the minimum value allowed by the fitting procedure), and an absorption-corrected luminosity of $\log L_{2-10 \text{ keV}}/\text{erg s}^{-1} = 45.63_{-0.24}^{+0.58}$. The best-fit model has a Cash statistic of $C = 56.3$ for $\nu = 65$ degrees of freedom. For W0220+0137, the best-fit model has $N_{\text{H}} = 3.5_{-3.2}^{+u} \times 10^{25} \text{ cm}^{-2}$ (where $+u$ signifies that the parameter is bound by the maximum value allowed by the fitting procedure) and $\log L_{2-10 \text{ keV}}/\text{erg s}^{-1} = 45.79_{-0.49}^{+0.12}$, with $C = 26.34$ and $\nu = 16$. Given the low number of counts for W0220+0137, Figure 9 shows the confidence regions for the two parameters to highlight the degeneracies between them. The best-fit values of N_{H} and $L_{2-10 \text{ keV}}$ are consistent within the uncertainties with those found by Vito et al. (2018) for both sources. The best-fit values for W0220+0137 are also consistent within the (large) error bars with those found by Goulding et al. (2018). For W0204–0506, A16 found that the best-fit absorbed AGN has $N_{\text{H}} = 0.63_{-0.21}^{+0.81} \times 10^{24} \text{ cm}^{-2}$, $\Gamma = 1.6_{-0.0}^{+0.8}$, and $\log L_{2-10 \text{ keV}}/\text{erg s}^{-1} = 44.9_{-0.14}^{+0.86}$, with $C = 66.08$ and $\nu = 77$.

The spectra of all three objects are likely dominated by a luminous AGN with very high absorption. In the case

of W0116–0505 and W0220+0137, the absorption is consistent with the objects being Compton-thick (i.e., $N_{\text{H}} > 1.5 \times 10^{24} \text{ cm}^{-2}$). This is in qualitative agreement with the SED modeling presented in Section 2.1. From the SED model of each object we can estimate the rest-frame intrinsic (i.e., obscuration-corrected) specific luminosity at $6 \mu\text{m}$, $L_{6 \mu\text{m}}$, which has been shown to be well correlated with the $L_{2-10 \text{ keV}}$ X-ray luminosity by a number of authors (Fiore et al. 2009; Gandhi et al. 2009; Bauer et al. 2010; Mateos et al. 2015; Stern 2015; Chen et al. 2017). We use the best-fit relation of Stern (2015) between $L_{6 \mu\text{m}}$ and $L_{2-10 \text{ keV}}$, which accurately traces this relation up to very high $L_{6 \mu\text{m}}$ and is hence most appropriate for our targets. From the $L_{6 \mu\text{m}}$ of the most luminous and obscured AGN component of W0116–0505, this relation predicts $\log L_{2-10 \text{ keV}}^{\text{Predicted}}/\text{erg s}^{-1} = 45.53 \pm 0.62$, which is in excellent agreement with the luminosity of the best-fit model to the X-ray data of $\log L_{2-10 \text{ keV}}/\text{erg s}^{-1} = 45.63_{-0.24}^{+0.58}$. For W0220+0137 we also find excellent agreement, with $\log L_{2-10 \text{ keV}}^{\text{Predicted}}/\text{erg s}^{-1} = 45.58 \pm 0.62$ and $\log L_{2-10 \text{ keV}}/\text{erg s}^{-1} = 45.54_{-2.16}^{+0.30}$. A16 nominally found a good agreement as well for W0204–0506, as they estimated $\log L_{2-10 \text{ keV}}^{\text{Predicted}}/\text{erg s}^{-1} = 45.36 \pm 0.37$ and found $\log L_{2-10 \text{ keV}}/\text{erg s}^{-1} = 44.9_{-0.14}^{+0.86}$ from the best-fit X-ray model. However, when jointly considering this with the best-fit and expected absorption, their Figure 5 suggests W0204–0506 may be somewhat X-ray weak. We remind the reader, nonetheless, that the error bars derived for our $L_{6 \mu\text{m}}$ estimates could be underestimated when considering the minimalist approach used for the SED

modeling in Section 2.1, which may make the disagreement less significant.

From the SED modeling we also have an estimate of the amount of dust that is obscuring the luminous AGN that dominates in both the mid-IR and the X-rays. Comparing to the column densities of neutral hydrogen constrained by the modeling of X-ray spectra, we find dust-to-gas ratios of $E(B - V)/N_{\text{H}} = 3.5 \pm 2.0 \times 10^{-24} \text{ cm}^2 \text{ mag}$ for W0116–0505, where the uncertainty corresponds to the 68.3% confidence interval and has been derived, for simplicity, assuming Gaussian statistics. For W0220+0137 we find $E(B - V)/N_{\text{H}} = 2.3 \times 10^{-24} \text{ cm}^2 \text{ mag}$. As N_{H} is not constrained at the 90% level within the model boundaries, we cannot derive a meaningful confidence interval. For W0204–0506, A16 found a larger ratio of $E(B - V)/N_{\text{H}} = 1.54 \pm 1.26 \times 10^{-23} \text{ cm}^2 \text{ mag}$. For comparison, the median dust-to-gas ratio in AGN found by Maiolino et al. (2001) is $1.5 \times 10^{-23} \text{ cm}^2 \text{ mag}$. This value is comparable to that found in W0204–0506, while those found in W0116–0505 and W0220+0137 are lower. Unfortunately the large uncertainties in this quantity make this result difficult to interpret, but it is worth noting that recently Yan et al. (2019) identified a very low dust-to-gas ratio of $\approx 4 \times 10^{-25} \text{ cm}^2$ for a heavily obscured nearby quasar at $z = 0.218$ with $N_{\text{H}} \approx 3 \times 10^{25} \text{ cm}^{-2}$, with around $N_{\text{H}} \approx 10^{23} \text{ cm}^{-2}$ coming from the ISM, which could be a better analog to our objects. If the dust-to-gas ratio is indeed significantly lower in W0116–0505 and W0220+0137 than in W0204–0506, it could either imply a low metallicity for the former systems such that there is a deficit of dust overall in the host galaxy, or that a higher than typical fraction of absorbing gas exists within the dust sublimation radius of the accretion disk. We speculate the latter could be consistent with the recent results of Wu et al. (2018) that show Hot DOGs are accreting close to the Eddington limit, perhaps as a result of higher gas densities in the vicinity of the SMBH.

Taken together, these results could imply that W0116–0505 and W0220+0137 represent a different class of object than W0204–0506, as the former are either dust-poor or gas-rich in the nuclear regions, but have normal X-ray luminosities, while the latter has a normal amount of dust but might be somewhat X-ray weak. The morphology of the HST imaging strongly differs between these objects, as discussed in Section 2.3, further supporting this. Goulding et al. (2018) points out that W0220+0137 is also classified as an ERQ by Hamann et al. (2017), and finds that W0116–0505 fulfills most of the criteria and hence classifies it as ERQ-like. This supports a view in which ERQs and Hot DOGs are not independent populations, but possibly related to each other with BHDs being the link between them. We speculate that Hot DOGs might correspond to the highly obscured AGN phase of galaxy evolution proposed by, e.g., Hopkins et al. (2008) or Alexander & Hickox (2012), and as the obscuration starts clearing out (see Hickox & Alexander 2018, for a description of the different physical scales of the obscuring materials), the object transforms into a BHD and then an ERQ, before transitioning into an unobscured quasar. The significant levels of outflowing ionized gas identified by Zakamska et al. (2016) for four ERQs, by Díaz-Santos et al. (2016) for the most luminous Hot DOG, W2246–0526, and by Wu et al. (2018) for two more Hot DOGs, support the view that both types of objects are experiencing strong AGN feedback.

4. Source of the Excess Blue Emission

4.1. Dual AGN

One of the possible scenarios proposed by A16 is that BHDs could be powered by two AGNs instead of one, where a primary luminous, highly obscured AGN dominates the mid-IR emission, and a secondary fainter, unobscured or lightly obscured AGN dominates the UV/optical emission. As can be seen in Table 2, the putative secondary AGN has a much lower ($\lesssim 1\%$) best-fit monochromatic luminosity at $6 \mu\text{m}$ in all three targets. As discussed above, the former would be expected to dominate the hard X-ray emission of these sources, and that is exactly what is observed. However, the less luminous component would contribute significant soft X-ray emission, which can be constrained by the Chandra observations. In Table 2 we list the expected intrinsic $6 \mu\text{m}$ luminosity of the primary and secondary best-fit AGN components for both W0116–0505 and W0220+0137. It is important to note that for the secondary AGN components we have no useful constraints in the infrared, as the rest-frame near-IR is dominated by the host galaxy and the mid-IR is dominated by the primary AGN component. Its $6 \mu\text{m}$ luminosity comes instead indirectly from the template fit to the rest-frame UV/optical SED. Furthermore, there could be neglected systematic uncertainties, as discussed at the end of Section 2.1. As we did in Section 3, we can estimate the expected 2–10 keV luminosity using the relation of Stern (2015). Hence, if the secondary component is a real second AGN in the system, for W0116–0505 we expect it to have an X-ray luminosity of $\log L_{\text{Predicted, 2-10 keV}}/\text{erg s}^{-1} = 44.43 \pm 0.37$, and for W0220+0137 we expect it to have $\log L_{\text{Predicted, 2-10 keV}}/\text{erg s}^{-1} = 44.29 \pm 0.62$. The gray-dashed curves in Figures 6 and 8 show the expected X-ray spectrum of these secondary components for W0116–0505 and W0220+0137 respectively. We assume power-law spectra with $\Gamma = 1.9$ and no absorption, as both secondary components show no reddening in the UV/optical. Figure 7 also shows the expected X-ray spectrum of the secondary AGN, as determined from the analysis of A16.

If we add a secondary power-law component to the X-ray spectral fit, we can place 90% upper limits on the luminosity of these power-law components of $\log L_{\text{2-10 keV}}/\text{erg s}^{-1} < 43.95$ in W0116–0505, and of $\log L_{\text{2-10 keV}}/\text{erg s}^{-1} < 43.93$ in W0220+0137. These limits are marginally consistent with the 2–10 keV luminosities expected given the optical/UV luminosities observed. For W0204–0506 on the other hand, A16 was able to rule out this scenario with high confidence. Unlike the analysis presented here, A16 reached this conclusion by comparing the change in Cash statistic of the X-ray spectra modeling obtained by requiring or not requiring the presence of the secondary AGN emission with the expected luminosity. Specifically, A16 found that including the secondary component resulted in an increase in the Cash statistic, $\Delta C = 128.38$, which allowed them to rule out the dual AGN scenario with $>99.9\%$ confidence. We do not replicate this analysis for W0116–0505 and W0220+0137, as the interpretation of the change in the C statistic ($\Delta C = 17.3$ and $\Delta C = 18.7$, respectively) is complicated by the lower number of counts detected, particularly in the case of W0220+0137, and hence we cannot assume Gaussian statistics.

Hence, the X-ray spectra of all three objects are better described by the single, highly absorbed AGN model, suggesting that BHDs are not dual AGN. The case is strongest

for W0204–0506, while for W0116–0505 and W0220+0137 we cannot completely reject the dual AGN scenario with high confidence using the current data sets.

4.2. Extreme Star Formation

Another possibility discussed by A16 is that the UV/optical SED of BHs is powered by unobscured extreme star formation rather than by unobscured AGN emission. This would account for a very blue UV/optical SED without the X-ray contribution expected for a secondary AGN.

This scenario was studied in detail by A16 for W0204–0506. Modeling the UV/optical SED of this object using the Starburst99 v7.0.0 code (Leitherer et al. 1999, 2010, 2014; Vázquez & Leitherer 2005) in combination with the EzGal package of Mancone & Gonzalez (2012), they determined that the SED could be consistent with it being powered by a young starburst but only if the SFR was very high. Specifically, they assumed the latest Geneva models available for the used version of Starburst99 (see Leitherer et al. 2014, for details), a constant SFR, and a solar metallicity, and determined that the SED could only be powered by a starburst of age $\lesssim 5$ Myr with $\text{SFR} \gtrsim 1000 M_{\odot} \text{ yr}^{-1}$ with 90% confidence. A lower metallicity somewhat eases these constraints, with the lowest metallicity available for the Geneva models in Starburst99 of $Z = 0.001$ implying age $\lesssim 100$ Myr and $\text{SFR} \gtrsim 250 M_{\odot} \text{ yr}^{-1}$. However, A16 considered that such a low metallicity was unlikely given the large amount of dust available in the inner regions of the system that give rise to the high specific luminosities in the mid-IR. Furthermore, due to the large, unobscured SFR implied by the solar metallicity models, A16 considered that the UV/optical SED was unlikely powered by a starburst.

However, the morphology of the UV emission in the HST imaging we have obtained (see Section 2.3 for details) seems to imply that starburst activity is present in W0204–0506. As shown in Figure 5, the flux traced by the F555W band (rest frame $\sim 1750 \text{ \AA}$) is distributed along the NE section of the galaxy and concentrated in a few distinct regions. The bulk of the F555W emission is considerably offset from the emission of the older stars traced by the F160W band (rest frame $\sim 5100 \text{ \AA}$). Furthermore, the morphology of the system is consistent with a merger (see Section 2.3), which can trigger significant star formation activity.

The analysis of A16 in conjunction with the HST imaging available for W0204–0506 then implies that if its UV/optical SED is solely powered by a starburst, then the system must be in a very uncommon state. It could be that the system has a very large metallicity gradient, such that in the outskirts, where star formation dominates, the metallicity is close to primordial and the SFR is only $\gtrsim 250 M_{\odot} \text{ yr}^{-1}$, yet near the SMBH the metallicity is high enough to allow for the substantial amount of dust needed to obscure the hyperluminous AGN. Another possibility would be that W0204–0506 does not have a substantial metallicity gradient but is instead powered by the strongest unobscured starburst known with $\text{SFR} \gtrsim 1000 M_{\odot} \text{ yr}^{-1}$.

A third and more likely option is that while a moderate starburst is ongoing in the system, the UV/optical emission is still dominated by light leaking from the central highly obscured AGN. As shown in Table 3 (also see the discussion in Section 2.3), the light distribution of W0204–0506 in the F555W band has a somewhat larger Gini and a significantly larger M_{20} coefficient than the other two BHs studied. While

the large M_{20} is consistent with the observed patchiness of the system, the high Gini coefficient implies that the light is strongly concentrated in the brightest regions. In the left panel of Figure 5, it can be appreciated that the NW UV clump (marked by the magenta arrow) is brighter than the rest, containing approximately 10% of the total F555W flux measured in the $4''$ radius aperture. This region is close to the geometrical center of the F160W light distribution, and could correspond to the position of the buried AGN. That the optical spectrum of this source (Figure 3) shows a mixture of narrow and broad emission lines is also consistent with this picture, as A16 reported a FWHM of $1630 \pm 220 \text{ km s}^{-1}$ for C IV but of only $550 \pm 100 \text{ km s}^{-1}$ for C III].

For W0116–0505 and W0220+0137 the situation is somewhat different. The optical spectra, shown in Figures 2 and 4, show clear broad, high-ionization features characteristic of quasars. The UV emission, while spatially extended, is strongly concentrated in both objects (see the discussion in Section 2.3), which is more consistent with the expectations for the dual AGN or the leaked AGN light scenarios, instead of the star formation scenario. We model the broadband SEDs of these objects as starbursts as in A16, but with a small modification. As the approach of A16 only models the continuum emission, we add to the Starburst99 models the emission lines of the spectra presented in Section 2. Each emission line was modeled using a single Gaussian profile after subtracting a local continuum estimated with a linear interpolation from the continuum regions immediately blueward and redward of the emission line in question. The only exceptions to this are Ly α and N V, for which the continuum was only modeled using the continuum region immediately redward of them, as the blue continuum is affected by Ly α forest absorption. A single Gaussian profile is a good model of the N V, C IV, He II, and C III] emission, as well as for the S IV+O IV] line complex. For Ly α we recover the majority of the flux in both objects, but the peak of the best-fit Gaussian falls somewhat short of their observed narrow peak. The best-fit models are shown in Figures 10 and 11 for W0116–0505 and W0220+0137, respectively. Each figure shows the best fit obtained assuming a solar metallicity and a metallicity of $Z = 0.001$, as discussed above. As we do not include additional nebular emission or Ly α forest absorption, we only use the bands that are redward of the Ly α emission line and exclude the F160W band, which can be strongly contaminated by an older stellar population and by nebular [O II] emission (which could be broadened and have a high equivalent width, as found by Jun et al. 2020 for a different group of Hot DOGs). Indeed, if we include the F160W band, we find best-fit χ^2 values a factor ~ 3 larger. We set a minimum photometric uncertainty of 0.05 mag, as systematic differences between the measurements are unlikely to be below that level. In practice, this only affects the uncertainty used for the F555W band. The best-fit SFR, age, and obscuration of the stellar population are shown in the figures as well; however, the values are quite degenerate as shown in Figure 12, particularly as there are no constraints longwards of $\sim 4000 \text{ \AA}$. The only other longer wavelength broad bands that we have are in regions of the SED dominated by either an older stellar population or by the highly obscured, luminous AGN as shown in Figure 1, and hence are not useful for constraining these fits. We note, however, that the χ^2 values of the best fits are quite large when it is considered that we are fitting three different parameters. This, coupled with

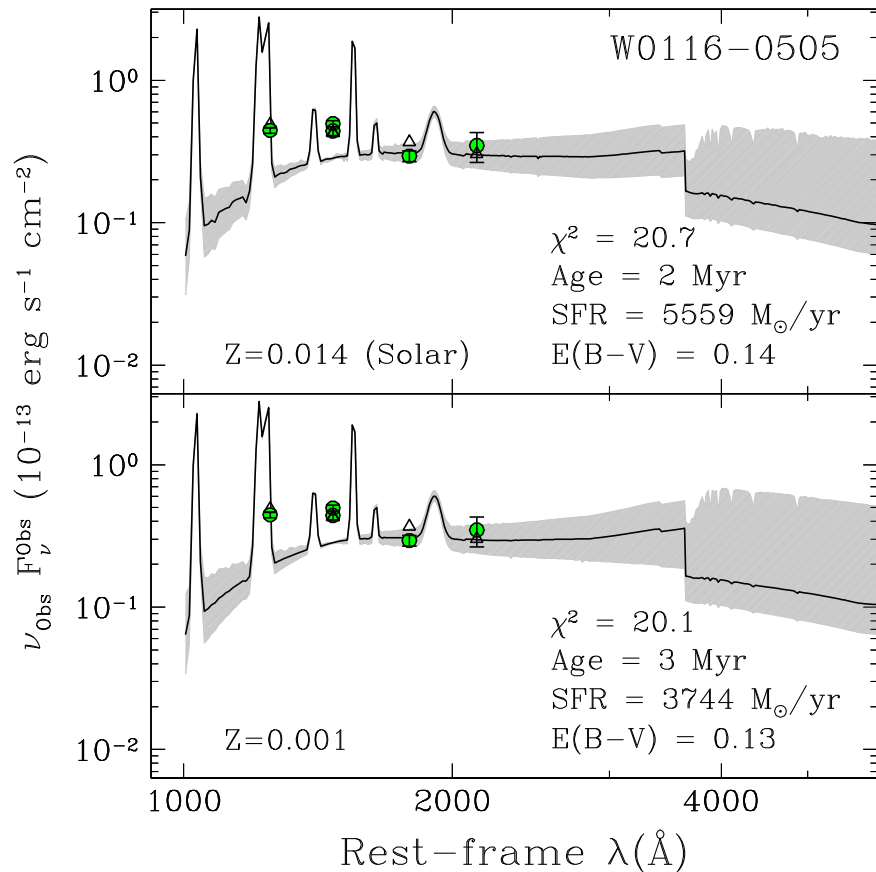


Figure 10. (Upper panel) The solid black line shows the best-fit Starburst99 SED model to the UV/optical broadband photometry of W0116–0505, assuming solar metallicity (see text for details). The gray shaded area shows all SED shapes within the 90% confidence interval. (Bottom panel) Same as in the top panel but for a metallicity of $Z = 0.001$.

UV/optical spectral features (i.e., the presence of broad emission lines) and the morphology in the HST imaging, suggests that it is unlikely that the UV/optical emission in these objects is dominated by unobscured starbursts.

4.3. Leaked AGN Light

The third possibility to explain the nature of BHDs is that the blue excess emission found in these objects corresponds to light coming from the highly obscured primary AGN that is leaking into our line of sight. As discussed by A16, this could happen either due to dust or gas scattering of the AGN emission into our line of sight, or due to a small gap in the dust that allows for a partial view toward the accretion disk and the broad-line region. However, the latter is unlikely, as discussed by A16, as the UV/optical SED is consistent with the emission of an unobscured accretion disk. As radiation at progressively shorter wavelengths is emitted in progressively inner regions of the accretion disk, a gap that only allows $\sim 1\%$ of the emitted light through but does not distort the accretion disk spectrum would need to cover 99% of the effective disk size at each wavelength. While not impossible, the shape of such a gap would be exceedingly contrived, making this unlikely. Furthermore, we would not expect the UV/optical emission to be spatially extended, as found in Section 2.3.

This suggests that the most likely source of the blue excess emission in the three BHDs studied here is scattered light. In this scenario, 99% of the emission from the accretion disk and the broad-line region would be absorbed by dust, while 1%

would be scattered into our line of sight by either dust or gas, or both. Reflection nebulae are known to make the reflected SED bluer than the emitted SED in the UV ($\lambda \lesssim 2500 \text{ \AA}$, e.g., see Draine 2003a), suggesting that the scattering medium in BHDs is more likely the gas surrounding the AGN. However, as there is likely dust on scales larger than the torus (Díaz-Santos et al. 2016; Tsai et al. 2018), we note that our data are not sufficient to rule out an SED that has been made bluer by dust reflection and redder by dust absorption. With respect to the X-rays, we note that while they should also be scattered into our line of sight along with the UV emission, the scattering cross section by either dust or free electrons is significantly smaller at the high energy ranges probed by the Chandra observations (Draine 2003a, 2003b). Hence, the nondetection of a clear unabsorbed component in the X-ray spectra in Section 3 is consistent with this scattering scenario.

5. Summary

We have investigated the source of the blue excess emission in three BHDs, two of which were identified as such by A16, and a third one which has an SED consistent with that of a Hot DOG, although it does not meet the formal selection criteria due to being slightly too bright in the W1 band. While all Hot DOGs are characterized by mid-IR emission that is most naturally explained by a highly obscured hyperluminous AGN (Eisenhardt et al. 2012; Assef et al. 2015; Tsai et al. 2015), BHDs have a UV/optical SED that is significantly bluer than expected based on template fitting results. Using a similar

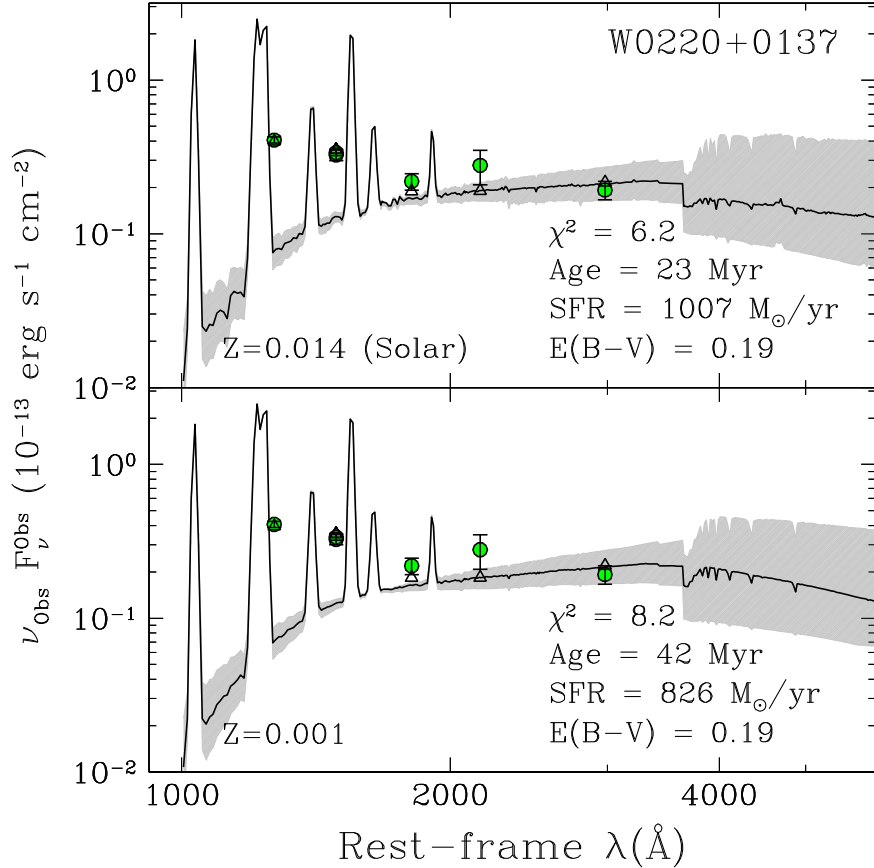


Figure 11. Same as Figure 10 but for W0220+0137.

approach to that of Assef et al. (2015), we find that the SEDs of BHDs are best modeled using two AGN components: a primary hyperluminous, highly obscured AGN that dominates the mid-IR emission, and a secondary lower luminosity but unobscured AGN that dominates the UV/optical emission. The bolometric luminosity of the secondary AGN SED is $\sim 1\%$ of that of the primary component (although, as discussed at the end of Section 2.1, there could be unaccounted systematic uncertainties in the luminosities due to our minimalistic SED modeling approach). A16 identified three possible scenarios to produce the excess blue emission, namely: (i) a secondary, less luminous but unobscured AGN in the system, (ii) an extreme starburst, or (iii) leaked UV/optical light from the primary, highly luminous, highly obscured AGN that dominates the mid-IR.

For one of the sources (W0204–0506), A16 ruled out a secondary AGN as the source of the blue excess emission, and instead concluded that the excess was caused by either unobscured star formation with an $\text{SFR} \gtrsim 1000 M_\odot \text{ yr}^{-1}$, or by UV/optical light from the central engine leaking into our line of sight due to scattering or through a partially obscured sight line, with the scattered AGN light hypothesis deemed more likely. In this paper, we have presented HST/WFC3 imaging of W0204–0506 showing a morphology consistent with an ongoing merger and evidence of an ongoing widespread starburst. Considering, however, the very high SFR needed to explain the UV emission by star formation alone, we conclude it is more likely that the UV emission of W0204–0506 arises from a combination of scattered AGN light and star formation.

We also studied in detail two other BHDs, W0116–0505 and W0220+0137. We present observations obtained with Chandra/ACIS-S and interpret them using the Brightman & Nandra (2011) models. We find that the X-ray spectra are consistent with single luminous, highly absorbed AGNs dominating the X-ray emission. We find that the $L_{2-10 \text{ keV}}$ luminosities of these AGNs are consistent with those expected for the primary AGNs based on their estimated $L_{6 \mu\text{m}}$ according to the $L_{6 \mu\text{m}} - L_{2-10 \text{ keV}}$ relation of Stern (2015). We also find that the gas-to-dust ratios of the AGNs in these systems are somewhat below the median value found in AGNs by Maiolino et al. (2001) and lower than that found in W0204–0506, suggestive of a lower metallicity or of a higher fraction of absorbing gas within the dust sublimation radius of the AGN. Based on the UV through mid-IR SED models of these sources, we estimate the expected X-ray luminosity of the putative secondary AGN components assuming it is a second, independent AGN in the system. We found that the X-ray observations are only marginally consistent with the presence of a second AGN component in both W0116–0505 and W0220+0137, suggesting the dual AGN scenario is unlikely.

We followed A16 and modeled the UV emission of W0116–0505 and W0220+0137 assuming a pure starburst scenario, and found that while the best-fit SFRs are generally high, comparable to those found by A16 for W0204–0506, they are not well constrained due to the large degeneracies between SFR, age, and metallicity. We found, however, that the χ^2 values of the best-fit starburst models are large (~ 12 for W0116–0505 and ~ 8 for W0220+0137) despite the small number of degrees of freedom (1 and 2, respectively), implying

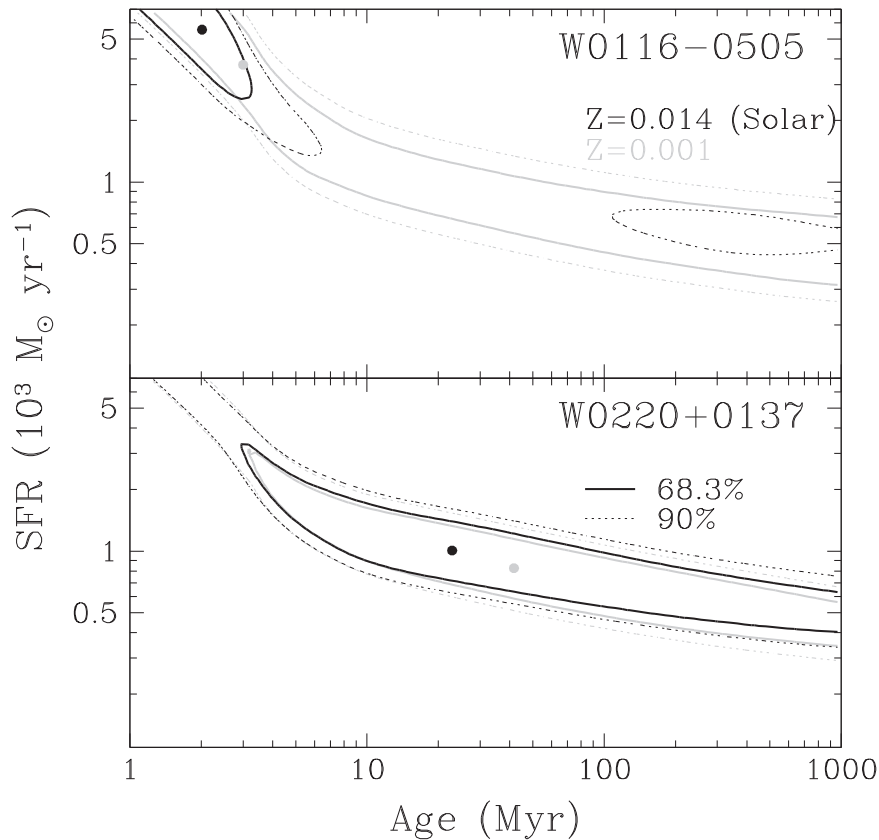


Figure 12. The contours show a χ^2 map of the best-fit Starburst99 models as discussed in the text. The contours for W0116–0505 and W0220+0137 are shown in the top and bottom panels, respectively. Dark contours assume solar metallicity, while gray contours assume $Z = 0.001$. The solid (dotted) contour shows the 68.3% (90%) confidence region, while the solid dots show the values of the best-fit models shown in Figures 10 and 11.

a pure starburst is not a good description of the observed UV SED. Additionally, the rest-frame UV spectra shows broad emission lines characteristic of AGN activity, further suggesting that star formation does not dominate the observed UV emission.

Finally, we also studied the morphologies observed in the HST/WFC3 F555W and F160W images of W0116–0505 and W0220+0137 and found them to be undisturbed with the UV emission being centrally concentrated. An analysis based on the Gini, M_{20} , and A coefficients showed that these systems are best characterized as undisturbed early-type galaxies, consistent with the leaked AGN scenario. Considering all of this, we conclude that the source of the UV emission in W0116–0505 and W0220+0137 is scattered light from the hyperluminous, highly obscured AGN that powers the mid-IR SED. Given the detail of our data and SED modeling, we cannot determine whether the scattering material is primarily gas, dust, or a mixture of both. As discussed in Section 3, W0220+0137 is classified as an ERQ and W0116–0505 is classified as ERQ-like (Hamann et al. 2017). Recently, Alexandroff et al. (2018) found high polarization fractions in the UV spectra of three ERQs, implying the UV emission has a strong contribution by scattered light from the central engine for these objects. This is highly consistent with our conclusions.

That all three BHDs we have investigated are due to scattered light from the highly obscured, hyperluminous AGN highlights how powerful the central engine is in Hot DOGs: with only 1% of the emission of the accretion disk scattered into our line of sight, it is still more luminous than the entire stellar emission of the host galaxy in the UV. This is in general

agreement with recent results that show that the SMBHs in Hot DOGs are accreting above the Eddington limit (Tsai et al. 2018; Wu et al. 2018) and are injecting large amounts of energy into the ISM of their host galaxies (Díaz-Santos et al. 2016), and hence are experiencing strong events of AGN feedback.

We thank J. Comerford and B. Weiner for carrying out observations presented in this article. We also thank the anonymous referee for the comments and suggestions to improve the manuscript. R.J.A. was supported by FONDECYT grant Nos. 1151408 and 1191124. D.J.W. acknowledges financial support from the STFC Ernest Rutherford fellowship. H.D.J. was supported by Basic Science Research Program through the National Research Foundation of Korea (NRF) funded by the Ministry of Education (NRF-2017R1A6A3A04005158). F.E.B. acknowledges support from CONICYT-Chile (Basal AFB-170002) and the Ministry of Economy, Development and Tourism’s Millennium Science Initiative through grant IC120009, awarded to The Millenium Institute of Astrophysics, MAS. T.D-S. acknowledges support from the CASSACA and CONICYT fund CAS-CONICYT Call 2018. J.W. is supported by the NSFC grant 11690024 and SPRP CAS grant XDB23000000. C.-T. was supported by a grant from the NSFC (No. 11973051). This work is based on observations made with the NASA/ESA Hubble Space Telescope, obtained at the Space Telescope Science Institute, which is operated by the Association of Universities for Research in Astronomy, Inc., under NASA contract NAS 5-26555. These observations are associated with program

#14358. Support for program #14358 was provided by NASA through a grant from the Space Telescope Science Institute, which is operated by the Association of Universities for Research in Astronomy, Inc., under NASA contract NAS 5-26555. The scientific results reported in this article are based to a significant degree on data obtained from the Chandra X-ray Observatory and observations made by the Chandra X-ray Observatory and published previously in cited articles. Support for this work was provided by the National Aeronautics and Space Administration through Chandra Award Number 17700696 issued by the Chandra X-ray Center, which is operated by the Smithsonian Astrophysical Observatory for and on behalf of the National Aeronautics Space Administration under contract NAS8-03060. This publication makes use of data products from the Wide-field Infrared Survey Explorer, which is a joint project of the University of California, Los Angeles, and the Jet Propulsion Laboratory/California Institute of Technology, funded by the National Aeronautics and Space Administration. This work is based in part on observations made with the Spitzer Space Telescope, which is operated by the Jet Propulsion Laboratory, California Institute of Technology under a contract with NASA. The Pan-STARRS1 Surveys (PS1) have been made possible through contributions of the Institute for Astronomy, the University of Hawaii, the Pan-STARRS Project Office, the Max Planck Society and its participating institutes, the Max Planck Institute for Astronomy, Heidelberg and the Max Planck Institute for Extraterrestrial Physics, Garching, The Johns Hopkins University, Durham University, the University of Edinburgh, Queen's University Belfast, the Harvard-Smithsonian Center for Astrophysics, the Las Cumbres Observatory Global Telescope Network Incorporated, the National Central University of Taiwan, the Space Telescope Science Institute, the National Aeronautics and Space Administration under grant No. NNX08AR22G issued through the Planetary Science Division of the NASA Science Mission Directorate, the National Science Foundation under grant No. AST-1238877, the University of Maryland, and Eotvos Lorand University (ELTE) and the Los Alamos National Laboratory. Funding for SDSS-III has been provided by the Alfred P. Sloan Foundation, the Participating Institutions, the National Science Foundation, and the U.S. Department of Energy Office of Science. The SDSS-III website is <http://www.sdss3.org/>. SDSS-III is managed by the Astrophysical Research Consortium for the Participating Institutions of the SDSS-III Collaboration including the University of Arizona, the Brazilian Participation Group, Brookhaven National Laboratory, Carnegie Mellon University, University of Florida, the French Participation Group, the German Participation Group, Harvard University, the Instituto de Astrofísica de Canarias, the Michigan State/Notre Dame/JINA Participation Group, Johns Hopkins University, Lawrence Berkeley National Laboratory, Max Planck Institute for Astrophysics, Max Planck Institute for Extraterrestrial Physics, New Mexico State University, New York University, Ohio State University, Pennsylvania State University, University of Portsmouth, Princeton University, the Spanish Participation Group, University of Tokyo, University of Utah, Vanderbilt University, University of Virginia, University of Washington, and Yale University. Some of the observations reported here were obtained at the MMT Observatory, a joint facility of the Smithsonian Institution and the University of Arizona.

ORCID iDs

- R. J. Assef <https://orcid.org/0000-0002-9508-3667>
 M. Brightman <https://orcid.org/0000-0002-8147-2602>
 D. J. Walton <https://orcid.org/0000-0001-5819-3552>
 D. Stern <https://orcid.org/0000-0003-2686-9241>
 F. E. Bauer <https://orcid.org/0000-0002-8686-8737>
 A. W. Blain <https://orcid.org/0000-0001-7489-5167>
 R. C. Hickox <https://orcid.org/0000-0003-1468-9526>

References

- Abraham, R. G., van den Bergh, S., & Nair, P. 2003, *ApJ*, **588**, 218
 Alexander, D. M., & Hickox, R. C. 2012, *NewAR*, **56**, 93
 Alexandroff, R., Strauss, M. A., Greene, J. E., et al. 2013, *MNRAS*, **435**, 3306
 Alexandroff, R. M., Zakamska, N. L., Barth, A. J., et al. 2018, *MNRAS*, **479**, 4936
 Assef, R. J., Denney, K. D., Kochanek, C. S., et al. 2011, *ApJ*, **742**, 93
 Assef, R. J., Eisenhardt, P. R. M., Stern, D., et al. 2015, *ApJ*, **804**, 27
 Assef, R. J., Kochanek, C. S., Brodwin, M., et al. 2010, *ApJ*, **713**, 970
 Assef, R. J., Walton, D. J., Brightman, M., et al. 2016, *ApJ*, **819**, 111
 Banerji, M., Alaghband-Zadeh, S., Hewett, P. C., & McMahon, R. G. 2015, *MNRAS*, **447**, 3368
 Barger, A. J., Cowie, L. L., Chen, C.-C., et al. 2014, *ApJ*, **784**, 9
 Bauer, F. E., Yan, L., Sajina, A., & Alexander, D. M. 2010, *ApJ*, **710**, 212
 Bennert, V. N., Auger, M. W., Treu, T., Woo, J.-H., & Malkan, M. A. 2011, *ApJ*, **726**, 59
 Bertin, E., & Arnouts, S. 1996, *A&AS*, **117**, 393
 Brightman, M., & Nandra, K. 2011, *MNRAS*, **413**, 1206
 Cash, W. 1979, *ApJ*, **228**, 939
 Chen, C.-T. J., Hickox, R. C., Goulding, A. D., et al. 2017, *ApJ*, **837**, 145
 Conselice, C. J. 2014, *ARA&A*, **52**, 291
 Cutri, R. M., Wright, E. L., Conrow, T., et al. 2012, Explanatory Supplement to the WISE All-Sky Data Release Products, Tech. Rep., <http://wise2.ipac.caltech.edu/docs/release/allsky/expsup>
 de Breuck, C., van Breugel, W., Röttgering, H., et al. 2001, *AJ*, **121**, 1241
 Díaz-Santos, T., Assef, R. J., Blain, A. W., et al. 2016, *ApJL*, **816**, L6
 Díaz-Santos, T., Assef, R. J., Blain, A. W., et al. 2018, *Sci*, **362**, 1034
 Draine, B. T. 2003a, *ApJ*, **598**, 1017
 Draine, B. T. 2003b, *ApJ*, **598**, 1026
 Eisenhardt, P. R. M., Wu, J., Tsai, C.-W., et al. 2012, *ApJ*, **755**, 173
 Fan, L., Han, Y., Fang, G., et al. 2016a, *ApJL*, **822**, L32
 Fan, L., Han, Y., Nikutta, R., Drouart, G., & Knudsen, K. K. 2016b, *ApJ*, **823**, 107
 Farrah, D., Petty, S., Connolly, B., et al. 2017, *ApJ*, **844**, 106
 Finkelstein, S. L., Rhoads, J. E., Malhotra, S., Pirzkal, N., & Wang, J. 2007, *ApJ*, **660**, 1023
 Fiore, F., Puccetti, S., Brusa, M., et al. 2009, *ApJ*, **693**, 447
 Gandhi, P., Horst, H., Smette, A., et al. 2009, *A&A*, **502**, 457
 Goulding, A. D., Zakamska, N. L., Alexandroff, R. M., et al. 2018, *ApJ*, **856**, 4
 Griffith, R. L., Kirkpatrick, J. D., Eisenhardt, P. R. M., et al. 2012, *AJ*, **144**, 148
 Hainline, K. N., Shapley, A. E., Greene, J. E., et al. 2012, *ApJ*, **760**, 74
 Hamann, F., Zakamska, N. L., Ross, N., et al. 2017, *MNRAS*, **464**, 3431
 Hickox, R. C., & Alexander, D. M. 2018, *ARA&A*, **56**, 625
 Hopkins, P. F., Hernquist, L., Cox, T. J., & Kereš, D. 2008, *ApJS*, **175**, 356
 Jun, H. D., Assef, R. J., Bauer, F. E., et al. 2020, *ApJ*, **888**, 110
 Leitherer, C., Eklöv, S., Meynet, G., et al. 2014, *ApJS*, **212**, 14
 Leitherer, C., Ortiz Otálvaro, P. A., Bresolin, F., et al. 2010, *ApJS*, **189**, 309
 Leitherer, C., Schaerer, D., Goldader, J. D., et al. 1999, *ApJS*, **123**, 3
 Lotz, J. M., Davis, M., Faber, S. M., et al. 2008, *ApJ*, **672**, 177
 Lotz, J. M., Primack, J., & Madau, P. 2004, *AJ*, **128**, 163
 Lupton, R., Blanton, M. R., Fekete, G., et al. 2004, *PASP*, **116**, 133
 Magorrian, J., Tremaine, S., Richstone, D., et al. 1998, *AJ*, **115**, 2285
 Maiolino, R., Marconi, A., Salvati, M., et al. 2001, *A&A*, **365**, 28
 Mancone, C. L., & Gonzalez, A. H. 2012, *PASP*, **124**, 606
 Mateos, S., Carrera, F. J., Alonso-Herrero, A., et al. 2015, *MNRAS*, **449**, 1422
 Petrosian, V. 1976, *ApJL*, **209**, L1
 Piconcelli, E., Vignali, C., Bianchi, S., et al. 2015, *A&A*, **574**, L9
 Rhodes, J., Refregier, A., & Groth, E. J. 2000, *ApJ*, **536**, 79
 Ricci, C., Assef, R. J., Stern, D., et al. 2017, *ApJ*, **835**, 105
 Stern, D. 2015, *ApJ*, **807**, 129
 Stern, D., Dey, A., Spinrad, H., et al. 1999, *AJ*, **117**, 1122
 Stern, D., Lansbury, G. B., Assef, R. J., et al. 2014, *ApJ*, **794**, 102

- Stern, D., Moran, E. C., Coil, A. L., et al. 2002, *ApJ*, **568**, 71
Tsai, C.-W., Eisenhardt, P. R. M., Jun, H. D., et al. 2018, *ApJ*, **868**, 15
Tsai, C.-W., Eisenhardt, P. R. M., Wu, J., et al. 2015, *ApJ*, **805**, 90
van Dokkum, P. G. 2001, *PASP*, **113**, 1420
Vázquez, G. A., & Leitherer, C. 2005, *ApJ*, **621**, 695
Vito, F., Brandt, W. N., Stern, D., et al. 2018, *MNRAS*, **474**, 4528
Wright, E. L., Eisenhardt, P. R. M., Mainzer, A. K., et al. 2010, *AJ*, **140**, 1868
Wu, J., Bussmann, R. S., Tsai, C.-W., et al. 2014, *ApJ*, **793**, 8
Wu, J., Jun, H. D., Assef, R. J., et al. 2018, *ApJ*, **852**, 96
Wu, J., Tsai, C.-W., Sayers, J., et al. 2012, *ApJ*, **756**, 96
Yan, W., Hickox, R. C., Hainline, K. N., et al. 2019, *ApJ*, **870**, 33
Zakamska, N. L., Hamann, F., Pâris, I., et al. 2016, *MNRAS*, **459**, 3144